UCRL-JRNL-228370

LAWRENCE
LIVERMORE
NATIONAL
LABORATORY

Mesoscale Heterogeneity in the Plastic Deformation of a Copper Single Crystal

K. R. Magid, J. N. Florando, D. H. Lassila, M. M. LeBlanc, N. Tamura, J. W. Morris Jr.

February 27, 2007

Philosophical Magazine

Disclaimer

This document was prepared as an account of work sponsored by an agency of the United States Government. Neither the United States Government nor the University of California nor any of their employees, makes any warranty, express or implied, or assumes any legal liability or responsibility for the accuracy, completeness, or usefulness of any information, apparatus, product, or process disclosed, or represents that its use would not infringe privately owned rights. Reference herein to any specific commercial product, process, or service by trade name, trademark, manufacturer, or otherwise, does not necessarily constitute or imply its endorsement, recommendation, or favoring by the United States Government or the University of California. The views and opinions of authors expressed herein do not necessarily state or reflect those of the United States Government or the University of California, and shall not be used for advertising or product endorsement purposes.

Journal name in full, Vol. X, No. X, Month 2004, xxx–xxx

Article Type

Mesoscale heterogeneity in the plastic deformation of a copper single crystal

K. R. MAGID†, J. N. FLORANDO‡, D.H. LASSILA‡, M. M. LEBLANC‡, N. TAMURA§, AND J. W. MORRIS, JR. †

† Dept. Materials Science and Engineering, Univ. California, Berkeley, CA 94720
‡ Lawrence Livermore National Laboratory, Livermore, CA 94551
§ Advanced Light Source, Lawrence Berkeley National Laboratory, Berkeley, CA 94720

*Corresponding author. Email: jwmorris@berkeley.edu

Abstract

The work reported here is part of a 'multiscale characterization' study intended to clarify the deformation pattern in a Cu single crystal deformed in compression. A copper single crystal was oriented for single slip in the (111)[$\bar{1}$01] slip system and tested to ~10% strain in uniaxial compression, using a specifically designed '6 degree of freedom' compressive test device to achieve uniaxial strain. The macroscopic strain field was monitored during the test by optical 'image correlation' methods that mapped the strain field with a spatial resolution of about 100 µm. The strain field was measured on orthogonal surfaces, one of which (the x-face) was oriented perpendicular to [1 $\bar{2}$1] and contained the [$\bar{1}$01] direction of the preferred slip system. The macroscopic strain produced is an inhomogeneous pattern of broad, crossed shear bands in the x-face. One, the primary band, lay parallel to (111). The second, the 'conjugate' band, was oriented perpendicular to (111) and contains no common slip plane of the fcc crystal. The mesoscopic structure of the inhomogeneous macroscopic deformation pattern was explored with selected area diffraction, using a focused synchrotron radiation polychromatic beam with a resolution of 1-3 µm. Areas within the primary, conjugate and primary + conjugate strain regions of the x-face were identified and mapped for their orientation, excess defect density and shear stress. The mesoscopic defect structure consisted of broad, somewhat irregular primary bands that lay nominally parallel to (111) in a almost periodic distribution with a period of about 30 µm. These primary bands were dominant even in the region of conjugate strain. There were also broad conjugate defect bands, almost precisely perpendicular to the primary bands that tended to bridge primary bands and terminate at them. The residual shear stresses were large (ranging to well above 500 MPa) and strongly correlated with the primary shear bands. The results are compared to the mesoscopic defect patterns found in Cu in etch pit studies done some decades ago.

Keywords:

AMS Subject Classification:

1 Introduction

Crystal plasticity is a heterogeneous process. The heterogeneity is ultimately due to the fact that crystals deform at the microscopic level through the motion of discrete dislocations on particular slip systems, and is exaggerated by the fact that these interact to create microscopic entanglements, slip bands and cellular patterns. But the heterogeneity extends to the intermediate (mesoscopic) and even to the macroscopic level, through the appearance of coarse slip bands, mesoscopic defect patterns and macroscopic shear bands.

While the basic features of heterogeneous plasticity are reasonably well known, there are few (if any) well-documented cases in which the deformation of a crystal has been characterized across the spectrum of length scales with sufficient detail to show how the various levels connect together. One reason is that such a characterization study is tedious and requires the sequential application of a number of different experimental apparatuses and techniques. A second reason is that, until recently, the multiscale characterization of even simple metals was not entirely practical. However, with the advent of such characterization techniques as 'image correlation', synchrotron radiation, electron backscatter diffraction (EBSD) and focused ion beam (FIB) machining, multiscale characterization is rapidly becoming both feasible and practical.

Multiscale characterization is both possible and increasingly important. Not only is the understanding of crystal plasticity technologically valuable in its own right, but recent developments in the computational modelling of crystal plasticity promise significant advances in the predictability of plastic deformation [1, 2]. However, the verification and refinement of these models, which are inherently multiscale in their form, requires that there be comparably well-characterized experimental examples.

The research that is reported here is part of a multiscale investigation of the deformation of a Cu single crystal that was oriented for single slip. The crystal was deformed in a customized facility that achieves nearly uniaxial compression. The 'macroscopic' strain that was developed during the test, which is, for our purposes, the average superficial strain over areas greater than about 100 μm in linear dimension, was measured and mapped continuously by 'image correlation'. After the sample had been strained in compression a bit over 10%, the 'mesoscopic' strain, the average strain over areas greater than ~1 μm in linear dimension, was measured and mapped by selected area diffraction in the focused white beam of a synchrotron light source. The residual stress and the defect density were measured simultaneously. The mechanical test device and the compression tests have been described elsewhere [3, 4]. The present paper is mainly concerned with the results of selected area diffraction. Complementary EBSD and supplementary transmission electron microscopic studies are underway to complete the multiscale characterization, and will be reported elsewhere.

Single-crystal copper was chosen for this research as a prototype material whose deformation behaviour has been extensively studied [5-10]. In particular, the mesoscopic dislocation patterns in Cu were characterized in some detail through etch-pit studies done by Livingston [11, 12] and Basinski [13] decades ago. These studies, and others on the plastic deformation of fcc single crystals [14-17], provide useful background for interpreting the results of the 'image correlation' and synchrotron studies reported here.

2 Experimental procedure

The sample used for this work was a copper single crystal, 99.99% pure that was grown via the Bridgman technique by Accumet, Inc. The crystal was cut by wire electrical discharge machining into a rectangular

parallelepiped like the one illustrated in Fig. 1, with a 5.5 mm square base, a 15 mm height and rounded edges. The longitudinal faces of the sample were cut perpendicular to the [$\bar{2}$ 9 20] direction so that the sample would be oriented for single slip on the primary slip system, (111)[$\bar{1}$01], when loaded in uniaxial compression. The lateral faces were cut perpendicular to [1 $\bar{2}$1] (the x-face) and [49 22 $\bar{5}$] (the y-face), to create the geometry shown in the figure. Fig. 2 includes a stereographic projection relative to the longitudinal axis, and also contains a table of calculated Schmid factors for the common fcc slip systems when the sample is compressed in this orientation.

The sample was deformed in nominally uniaxial compression in the '6DOF' apparatus at the Lawrence Livermore National Laboratory (LLNL). This apparatus is illustrated in Fig. 3 and is described in refs. [4, 18, 19]. It was designed to allow motion in six independent modes so that uniaxial compression would be essentially unconstrained. In this device a nominal point load is applied to a half-sphere that serves as the upper platen on the specimen. The lower platen rests on a set of ball bearings on a plane base. The upper half-sphere allows displacement along the vertical z-axis and rotation about the x- and y-axes (tilt in the zx- and zy-planes), while the mobile base allows displacement in the x or y directions and rotation about z (twist in the xy basal plane). If the loading mechanism and bearings are frictionless, the deformation path is uniaxial compression. The extent to which that condition pertains in the actual tests described here is discussed in ref. [4] and in the following.

The macroscopic strain was measured and mapped using a GOM Aramis 3-D imaging system (acquired from Trillion Quality Systems). This device measures the local strain by locating the positions of a distribution of microdots placed on the surface of the specimen. The positions are recorded in a CCD camera, and successive images are compared to measure local displacements and calculate displacement gradients ('image correlation' [20]). In the present case, angled pairs of cameras are focused on two orthogonal surfaces of the specimen during the test [21]. The angled pair provides a stereo view that is used to measure microdot displacements both in and normal to the surface plane. The two camera sets provide simultaneous strain measurements on orthogonal surfaces.

Image correlation was used to follow the strain in real time during the compression test. The overall strains were computed from averages taken over the sample surfaces. The data were recorded both as a data set and as a movie. A succession of still images from the movie is shown in Fig. 4, which includes colour-coded maps of the deformation on the x- and y-faces as a function of strain at a strain rate of 10^{-3}/sec. The test was terminated when the axial engineering strain reached 10.28%. There is, of course, some relaxation when the sample is removed from the apparatus. Direct comparison of maps taken in the loaded and unloaded conditions show that, in the present case, the relaxation is small and the strain maps are practically indistinguishable.

Following deformation, 1 mm thick sections were cut parallel to the x- and y-surfaces of the specimen by electro-discharge machining (EDM) (Fig. 5). The sectioned samples were used for the x-ray diffraction analyses reported here. The residual surfaces of the samples were used for a parallel characterization study, using EBSD that will be reported separately when it is completed [22]. The surfaces of the sectioned samples (which match those left on the original crystal) were prepared for x-ray analysis by polishing flat with 0.5 µm diamond.

As can be seen in the strain maps in Figs. 4 and 5, and will be discussed further below, the [1 $\bar{2}$1] (x-face) of the deformed crystal contained several distinguishable regions with distinct deformation patterns. To

locate these regions three platinum markers were placed on the sample surface. These are shown in Fig. 6. The markers could be found by x-ray microfluorescence during x-ray analysis and identified by their distinct shapes. The areas that were surveyed by the x-ray scans reported here were located by reference to the arrowhead on the central platinum marker.

The x-ray diffraction analyses were done on beamline 7.3.3 of the Advanced Light Source at the Lawrence Berkeley National Laboratory (ALS/LBNL). This particular instrument was well suited for these studies because of the high brilliance of its synchrotron source, the focusing optics that produce an ultrafine beam size, its "white beam" capabilities and the positioning stages that allow the beam to be swept with a micro-scale step size over a one square centimetre area. In the tests described here a polychromatic (white) x-ray beam from a bending magnet source was focused to a spot size of approximately 0.8x1.2 micron full width at half-maximum (VxH) by a pair of elliptically bent Kirkpatrick-Baez mirrors. The sample was set in a reflective geometry at 45 degrees to the incident beam. The diffracted x-rays were collected with a large area Mar x-ray CCD detector (MAR133, collection area 13.3 cm diameter) that was positioned at an angle of 45 degrees approximately 3 cm from the specimen. An exposure time of 1 second was used for all experiments. Other beamline parameters were set to obtain high intensity reflections but avoiding peak saturation on the CCD. A Ge ORTEC solid-state detector coupled with a multichannel analyzer also permits the collection of fluorescence signals for elemental mapping. Further details of the beamline setup can be found elsewhere [23-25].

The areas that were scanned were chosen to provide meaningful data in the limited beam time available. The crystal was mounted on a 6-circle Huber diffractometer, the central, arrow-shaped platinum mark was found by microfluorescence and the area of interest was located by displacement from the tip of the arrow. The area was scanned with a step size of 1-3 microns. The initial experiments used a step size of 3 microns to map three selected areas on the surface of the $[1\ \bar{2}1]$ face of the crystal. A square with a 297 µm edge was mapped in the central region of the crystal while squares of 180µm size were scanned at selected sites in the upper and lower regions. In subsequent sessions, a 0.030x9.592 mm^2 area down the centre of the crystal was mapped with a 2-micron step size to clarify the differences between the 3 initial scans and analyze the transitions between visually different regions on the crystal surface. In addition, two 50 µm x 50 µm regions were scanned with a one micron step size to provide the best resolution in the top 'dead-zone' portion of the crystal and in the central region of the crystal. The final set of scans mapped additional areas in each of 3 distinct regions of the crystal with a 2 µm step size.

The data taken in these diffraction experiments are Laue diffraction patterns that sample an area roughly equal to the diameter of the focused beam (~ 1 µm) to a depth that approximates the penetration depth of the beam (~ 30 µm). The diffraction patterns were analyzed with XMAS (X-ray Microdiffraction Analysis Software), which was written in-house for the beamline at the ALS [26, 27]. Laue patterns from unstrained copper and silicon reference samples were used as reference patterns for the analysis of the deformed sample. The patterns from the unstrained reference samples are used in the XMAS software to calibrate geometric parameters of the beamline during each session.

The measured Laue diffraction patterns contain three types of data. First, the average overall orientation of the sampled volume is measured from the orientation of the diffraction pattern. This data was used to map the total rotation from the original orientation of the specimen, and the misorientation of adjacent volumes within the specimen. Second, the misorientation within the sampled volume is measured by the half-width of the diffraction peaks. This misorientation is ordinarily due a local excess density of the dislocations whose

Burgers vectors accomplish the deformation and, hence, provides a measure of the 'geometrically necessary' dislocation density [28]. Third, the average deviatoric strain within the sampled volume is measured by the distortion of the diffraction pattern. The deviatoric stress tensor is computed from the strains using the anisotropic elastic constants of the material and was used to calculate the Von Mises (shear) stress, the maximum shear stress, and the resolved shear stresses on the preferred slip systems. Examples are presented in the following. Given the beamline geometric parameters, the expected accuracy in the orientation matrix is $\pm$ 0.01º and the accuracy in the strain tensors is $\pm$ 1×10^{-4} respectively [23, 27]. These are, of course, averages over the sampled volume.

We note that the orientation data can be obtained more rapidly, and with better spatial resolution, with modern EBSD techniques. However, the orientations are much more accurately determined with the methods used here, and the dislocation densities and residual stresses are difficult to extract from EBSD data. To compare the two methods more specifically, a parallel EBSD study is underway using the matching faces to the samples studied here [22].

3 Results and Discussion

3.1 Macroscopic strain patterns

The sample studied here was oriented for easy glide on the (111)[$\bar{1}$01] system when loaded in uniaxial compression and was tested in the 6DOF fixture at LLNL. The engineering stress-strain curve from the test is in Fig. 4. The sample yielded at about 16 MPa. It deformed in 'easy glide' to a strain of about 0.025 and afterwards hardened almost linearly to the final strain, ~ 11.4%, where the test was terminated. The stress-strain data from this and other tests is discussed in more detail in ref. [29]. The yield strength of this sample was high compared to that measured in other tests and reported by other investigators [29]. The reason appears to be that this crystal was tested in the as-cut condition, and residual defects from the EDM machining strengthened the crystal. However, the hardening behaviour and deformation patterns in this crystal were qualitatively the same as those observed in annealed crystals with lower strength.

The pattern of deformation during the compression test is shown as a function of strain in the sequence of image correlation maps of the axial strain (ε_{yy}) in Fig. 4. These were taken from films made during the test. The interesting behaviour occurs in the x-face (perpendicular to [1 $\bar{2}$1]). During the 'easy glide' stage of deformation the strain develops in a band on the x-face at 45º to the compression axis (z-axis), and gradually intensifies. This deformation band parallels the trace of the (111) glide plane and will be referred to as the 'primary' band.

A well-defined 'conjugate' deformation band also forms, with an orientation 90º from the primary. This conjugate band develops from the beginning of the test, and is visually obvious in the strain map when the compressive strain reaches about 2% (Fig. 4). This band also lies on a plane of maximum shear at 45º from the compression axis, but, significantly, this secondary shear plane contains none of the preferred slip systems for fcc copper. Both the primary and conjugate bands intensify as the strain increases, with the axial strain concentrated particularly in the central region of mixed deformation where the two bands cross.

Fig. 4 also traces the development of deformation on the y-face as a function of strain. On this face the strain is concentrated in essentially parallel bands, perpendicular to the compressive axis. At low strain these

are most pronounced in the lower area of the face, where the primary slip bands intersect this face. At higher strains horizontal deformation bands also decorate the upper area of the y-face. These bands correspond to intersections of the conjugate slip bands on the x-face.

Fig. 7 presents maps of all the strains on the x- and y-faces. On the x-face, the tensile strains ε_{zz} and ε_{yy} are pronounced. They have the same geometric pattern, but opposite signs (plastic deformation conserves volume and, therefore, tends to conserve area). The magnitude of the strain is slightly greater in the y-direction (ε_{yy}). There is, in addition, a significant shear strain, ε_{yz}, in the secondary deformation band on the x-face, but very little shear in the primary band. Local shears also appear at the upper left- and lower right-hand corners of the x-face, which suggest that there was some slight frictional deformation from the platens of the test fixture at these two positions. These local shears only appear in the last stages of deformation.

The stain field on the y-face is comparatively simple. The axial compression, ε_{zz}, is the only significant strain. Its pattern and magnitude appear to be consistent with the constraints that the total compression should be nearly the same on the x- and y-faces, and that volume should be conserved, with ε_{yy} slightly greater in magnitude than ε_{zz} on the x-face. There is a slight enhancement of ε_{zz} at the upper and lower edges of the y-face, and a slight indication of shear (ε_{xz}) on these edges.

3.2 Mesoscopic defect patterns

To characterize the mesoscopic defect patterns we used x-ray microdiffraction to map selected areas of the x- and y-surfaces. The scanned areas were selected to explore interesting features in the macroscopic strain maps.

3.2.1 Defect patterns on the y-face. We begin with a description of the defect patterns on the y-face, since these are much simpler than those on the x-face. Note that the traces of the preferred (111) slip plane are horizontal lines on the y-face, perpendicular to the z-axis of compression (Fig. 7), and that the preferred slip direction, $[\bar{1}01]$, has no x-component in the y-face. It follows that slip in the preferred system causes an out-of-plane deformation on the y-face in bands oriented perpendicular to the z-axis (the axis of compression). The slip system with the second largest Schmid factor is the $(\bar{1}11)[101]$. The trace of this slip plane makes an angle of about 30º to the horizontal in the y-face, and would cause slip in the x-direction, transverse to the plane.

The residual defect patterns that are revealed by microdiffraction on the y-face are shown in fig. 8. The insert figure on the left hand side of Fig. 8 shows the surface of the specimen. The macroscopic strain map obtained from image correlation is superimposed. Note that, as illustrated in the upper figure, the surface scanned was the inner surface of the cut layer, so the strain map that appears is the mirror image of that shown in fig. 4. The microdiffraction data is taken near the square indicated in the right centre of the face, in the region where the strain is most severe. Five data sets are plotted on the right-hand side of the figure.

The top figure (fig. 8a) is the 'out-of-plane' orientation map that shows the tilt of the y-face. The tilt appears in broad, irregular bands with well-defined edges. The bands are roughly perpendicular to the axis of compression and are 10-40 µm in width. They are also roughly periodic with a spacing of 30-40 µm. Morphologically, they resemble the heterogeneous bands of macroscopic strain on the surface of the specimen, and show that the heterogeneous pattern persists to much higher magnification. The roughly

constant angle within the bands shows that the 'geometrically necessary' defects that cause the tilt are concentrated along the edges of the bands. Note that the tilt angle is small; it changes by only about 1.5º over the whole area mapped. The fact that the bands are irregular, despite their clear edge definition may reflect participation by the secondary slip system, $(\bar{1}11)[101]$. The $(\bar{1}11)$ plane makes an angle of about 30º to the horizontal in the figure and is, hence, roughly parallel to the sloped edges of some of the orientation bands.

The second figure (Fig. 8b) is a map of the in-plane orientation over the same area. The orientation is, again, heterogeneous and banded in the direction perpendicular to the compression axis. Compared to the out-of-plane orientation pattern, the in-plane orientation bands are less well defined, their boundaries are more diffuse and the total misorientation is smaller, only abut 0.5º. Since the primary slip system does not produce displacement in the x-direction on this face, the in-plane misorientation bands must reflect the participation of secondary slip systems. This may explain the relative lack of definition of the bands.

Figs. 8c and 8d are local measures of misorientation. Fig. 8c maps the misorientation between adjacent diffracted areas ('pixels' that are approximate squares 2 µm on a side). Fig. 8d maps the misorientation within the pixels, as reflected in the spread of the diffraction spots. Since the lattice misorientation is accomplished by crystal defects, particularly 'geometrically necessary' dislocations, both are measures of the dislocation density. The internal misorientation is the more direct measure since it is more local, and we have used it to define the excess dislocation density. A comparison of Figs. 8c and 8d shows that the two measures of misorientation are almost identical. As expected, the bands of high dislocation density are located along the well-defined boundaries of the out-of-plane deformation bands (Fig. 8a). The excess dislocation density within the high-density bands is in the range $6\text{x}10^{13} – 8\text{x}10^{13}$ m^{-2}, and is roughly an order of magnitude above the background value, ~ $1\text{x}10^{13}$ inside the orientation bands.

The distribution of shear stresses can also be extracted from the microdiffraction data. For example, Fig. 8e is an pixel-by-pixel map of the maximum resolved shear stress over the scanned region. Note that the maximum shear stress exceeds 500 MPa, and is far above the critical resolved shear stress for easy glide in this crystal (< 10 MPa). Comparison with fig. 8d shows that the bands of high shear stress generally coincide with the bands of high dislocation density. The high shear stress is likely associated with dislocation pile-ups and entanglements on the boundaries of the misorientation bands. There is, in fact, much more stress information contained in the microdiffraction data; the full deviatoric stress tensor can be calculated for each cell. Some of the additional data are presented below.

3.2.2 Defect patterns on the x-face. The slip vector of the primary slip system lies in the x-face of the crystal with the consequence that the heterogeneous defect patterns are most apparent in this face. The pattern is shown in the maps contained in Fig. 9. The insert figure on the right-hand side locates three areas that were scanned. The three areas are 180-300 µm on a side and are sited, respectively, just inside the broad band of primary strain, near the centre of the region of mixed primary and conjugate strain, and just inside the band of predominantly conjugate strain. Three data sets are mapped for each area: the in-plane orientation, the element-to-element misorientation and the internal misorientation (the excess dislocation density).

Despite their very different macroscopic strain features, the residual defect patterns are similar in the three areas sampled. In all three regions the in-plane orientation map is cross-hatched by broad bands with defined boundaries. The bands lie at roughly ± 45º to the z-axis (the axis of compression). The most pronounced bands lie roughly parallel to the (111) primary slip plane. The cross-hatched bands are on the conjugate shear plane, which does not parallel any close-packed plane of the fcc crystal, and appears to represent the

'polygonal slip' that was observed in the etch-pit studies of Livingston [11, 12] and Basinski [13]. The maximum in-plane misorientation is about 2.5º in the mixed and conjugate deformation regions, but only about 1º in the region of primary slip.

Local misorientation and dislocation density maps are presented in Figs. 9-10. As shown in Fig. 9, as expected, the excess dislocation density is concentrated in narrow bands that outline the orientation bands. Fig. 10 is a superposition of the local misorientation and dislocation density fields in the three regions. The distributions are essentially identical, showing that they are measuring essentially the same thing: the local value of the excess dislocation density. Fig. 10 also includes superimposed maps over three long strips, one taken in the primary deformation band, two in the mixed region of primary and conjugate shear. The defect distributions in the three regions have a surprisingly similar appearance given the very different macroscopic strain patterns. In all three regions the most pronounced defect bands are roughly parallel to the primary (111) slip plane and extend across the field of view. The primary bands are quasi-periodic with a separation of about 30 µm. They are somewhat irregular in shape, a feature that suggests the participation of secondary slip planes, particularly the $(\bar{1}11)$, whose trace is approximately 67º from the z-axis, and the $(11\bar{1})$, at about 22º from the z-axis. The perpendicular (conjugate) dislocation bands are more diffuse and less extended. They are present in all three regions, but are more common and pronounced in the mixed and the conjugate bands. They often connect primary bands and terminate on them. Fig. 11 includes Fourier transforms of a number of dislocation density distributions from each of the three regions, and shows that the primary and conjugate bands are almost precisely perpendicular. The measured excess dislocation densities in these high-density bands range up to about 6×10^{13} m^{-2}, against a background density of about 10^{12} m^{-2}.

Finally, Fig. 12 shows out-of-plane orientation maps taken over a number of areas, and along a strip that extends from the 'dead' region at the top of the crystal down to the bottom of the region of mixed deformation. Since the primary slip is in the x-plane, the out-of-plane misorientation must reflect slip on secondary systems. As the figure shows, the out-of-plane orientation maps are subdivided into bands that roughly parallel the primary deformation bands. This observation remains true even for scans taken well within the region of conjugate slip. The bands are, again, quasi-periodic with a period of about 30 µm. The misorientation across their boundaries is no more than about 0.5º. The long scan down the centre of the sample face shows that the crystal is very slightly bowed, possibly due to a small reaction at the platens during the later stages of the test.

3.3 Mesoscopic patterns of the residual stress

One of the attractive capabilities of microdiffraction as a characterization tool is its ability to measure the local value of the internal stress. In fact, the microdiffraction data reveals the full deviatoric stress tensor. In the following we discuss three measures of the stress: the in-plane shear stress, σ_{yz}, in the x-surface of the sample, the overall shear stress, as measured by the Von Mises stress, and the maximum resolved shear stress available to drive dislocation glide.

Fig. 13 includes a plot of the in-plane shear stress, σ_{yz}, in the x-face of the crystal. The shear stress is measured at intervals of 20 µm along the line indicated in the figure, which is plotted on the background map of the compressive strain. The mean value of the stress is very close to zero, as expected. Note the high values of the residual shear stresses. These reach several hundred MPa, which is far above the macroscopic shear stress applied during the compression test. As shown in Fig. 13(b) the values of the residual shear stress have a roughly Gaussian distribution with a standard deviation of about 100 MPa. The distribution of residual

shear stresses is roughly the same over the whole length of the crystal, despite significant differences in the magnitude and direction of the macroscopic strain from one region of the crystal to another. There is, however, a tendency for the highest residual stresses to be found in the transition regions where the macroscopic strain gradients have their largest values.

Fig. 14 shows the distribution of the Von Mises stress over the x-face. The left-hand side of the figure exhibits maps of the local distribution of stress over small, selected areas, 50-180 μm on the edge. The right-hand side shows the distribution of stress over 30x800 μm^2 strips taken in the three distinct regions of macroscopic strain.

The distribution of the Von Mises stress has three striking features. First, the Von Mises stress is surprisingly large. It exceeds 1 GPa in many locations within the crystal, far above the maximum value of the shear applied during the test.

Second, the local areas of very high stress, which are numerous, are organized into well-defined bands. The most pronounced of these bands parallel the primary bands of high dislocation density that were identified in the previous section. To emphasize this we have re-plotted data from Fig. 14 in Fig. 15, where they are placed alongside the corresponding plots of the dislocation density. As this figure makes clear, the high shear stress is within or in the immediate vicinity of the regions of high dislocation density; the high shear stress appears to be caused by dislocation activity and entanglements in the primary shear bands. High shear stresses are also found in bands along the conjugate shear directions, perpendicular to the primary bands. The stresses in these conjugate bands are, in general, less intense and more diffusely distributed than those in the primary bands. The association between the conjugate stress bands and the conjugate bands of high dislocation density is also a bit less clear.

Third, the bands of high residual stress tend to parallel the bands of primary slip, even in areas where conjugate slip dominates the macroscopic strain. Bands of stress do appear on conjugate planes with some frequency in the central (primary plus conjugate strain) and lower right (conjugate strain) regions, and are particularly common in the conjugate strain region. However, these are less intense and more diffuse than the bands in the primary direction. Moreover, particularly as shown by the maps in Fig. 14, they tend to connect primary bands and terminate on them, as if they were secondary features.

Finally, Figs. 16-18 illustrate the pattern of the maximum resolved shear stress (MRSS). The MRSS is the highest value of stress resolved on the 12 possible {111}/<110> dislocation glide systems in the fcc crystal. Fig. 16 presents maps of the MRSS over selected areas in the three distinct regions of macroscopic deformation. The MRSS patterns are very much like those of the Von Mises stress. The MRSS reaches high values (~ 600 MPa) and the high stresses are located predominantly in bands along the directions of primary shear. The MRSS is also high in conjugate bands oriented perpendicular to the primary bands. These bands tend to be weaker and more diffuse. They tend to connect the primary bands and terminate on them.

Fig. 17 includes maps that show the direction of the maximum resolved shear stress. Again the pattern follows the pattern of primary and conjugate bands. Interestingly, the highest stresses, which lie in the primary slip bands parallel to (111), are focused in directions, predominately [101], that do not lie in the (111) plane and would be difficult to relax by slip in (111). The maximum shear stress between bands tends to be focused in directions like $[0\ \bar{1}1]$ (orange) and $[1\ \bar{1}0]$ (red) that do lie in the (111) plane. These stresses

apparently could be relaxed by slip in (111), but the residual stress is very small; the stress has already been relaxed.

The pattern of stress concentration and relaxation is explored further in Fig. 18, on which we have superimposed plots of the MRSS and the dislocation density. The primary bands of high dislocation density superimpose almost precisely on the bands of MRSS. Interestingly, however, the conjugate bands of high dislocation density are not bands of high MRSS, even in the region where the macroscopic strain is dominated by conjugate slip. It appears that the primary dislocation bands tend to accumulate dislocations of the same sign, creating high residual stresses that cannot be relieved by glide in the slip plane. The conjugate dislocation bands predominate in regions of low stress, suggesting that these bands were formed in the process of relaxing shear stresses that could be relieved by primary slip.

4. Discussion

As discussed in the introduction, the work reported here had three purposes: to demonstrate a technique for multiscale characterization, to provide a characterized example of bulk deformation for comparison with simulation results and to clarify the mechanisms of plasticity in single crystal copper. The characterization studies done here stopped at the mesoscopic scale. The microscopic characterization of the dislocation processes that underlie these deformation patterns is in progress. We also note that the mesoscopic characterization was done on a single sample at a single macroscopic strain, about 10% axial compression.

Even in this simple case, uniaxial compression of an fcc Cu crystal oriented for single slip, deformation at all spatial scales involves heterogeneities that need to be taken into account if the overall deformation is to be understood. Moreover, the deformation patterns include features that are not obviously contained in the most widely accepted models of dislocation plasticity. Unanticipated patterns were found at both the macroscopic and mesoscopic levels.

4.1 Macroscopic behavior

The macroscopic strain field (the strain over areas of dimension greater than about 100 μm for our purposes) is heterogeneous, particularly over the x-face, and divides this face into several distinct areas with characteristic features. As expected, the strain field includes a broad, well-defined band of shear parallel to the (111) slip plane that contains the most highly stressed slip system (the highest Schmid factor). However, this shear is accompanied by a well-defined band of conjugate shear that is almost exactly perpendicular to (111). By symmetry, this conjugate plane experiences a shear stress equal to that on (111) (at least initially), but contains none of the preferred slip systems of fcc, and, hence, shear on this plane does not conform to the Schmid model. (We note that this behaviour is not unique to the particular crystal that was examined here; it is the common result of a number of uniaxial compression tests done on Cu crystals oriented for single slip.)

But at the same time that the deformation is more complex than anticipated, it remains relatively simple. The macroscopic strain field is not, at least superficially, a mixture of the many possible elementary slips. To a good first approximation, it is a simple superposition of two broad shear bands, one parallel to the slip plane that is expected from the Schmid model, and a second on the conjugate plane of maximum shear stress, as might be predicted on the basis of a macroscopic ‘slip-line’ model that ignored the crystallographic detail.

4.2 Mesoscopic defect patterns

Because the macroscopic strain had been mapped, it was possible to select areas for mesoscopic characterization that sampled regions with different macroscopic behaviour. We particularly explored areas within the primary, conjugate and overlapped strained regions on the x-face of the crystal. The selected area diffraction studies reveal stresses, rotations and excess dislocation densities at a resolution down to about 1 µm.

The heterogeneity and complexity of the deformation pattern increases at the mesoscale, but, interestingly, do not provide an obvious explanation for the conjugate shear bands that appear on the macroscale. The most striking feature in all three regions is a almost periodic pattern of thick, wavy bands that generally parallel to the primary (111) slip plane and are repeated about every 30 µm. Since these are the bands that are expected to carry the primary shear deformation, they should be present and dominant in the primary and mixed deformation regions. The (111) orientation of these bands is consistent with primary slip in the $(111)[\bar{1}01]$ slip system that has the maximum Schmid factor (Fig. 2). The waviness in the boundaries of the bands suggests some participation by secondary slip in the $(\bar{1}11)$ and $(11\bar{1})$ planes, as described in the previous section.

The primary deformation bands are connected or crossed by conjugate bands of defects that are relatively diffuse in appearance, but have an almost perpendicular orientation. These conjugate bands sometimes cross the primary bands to form a true cross-hatched pattern, but more commonly connect the extended, primary bands with short 'bridges' that terminate at both ends. This pattern suggests that the conjugate bands form after the primary bands and accommodate to them. The conjugate bands are present in all three regions, but are particularly common in the region of conjugate strain.

A mesoscopic defect structure composed of primary bands connected by secondary bands on perpendicular planes is a known pattern in deformed Cu that was first detected in the etch pit studies done by Livingston [15, 16] and Basinski [17] some fifty years ago. They studied single crystal Cu deformed in tension and bending at room temperature and at 4.2K, and observed a mesoscopic structure described as 'polygonized glide' in which primary bands of tangled dislocations roughly parallel to the preferred slip plane were joined by perpendicular, relatively diffuse secondary bands. Insofar as could be inferred from the character of the etch pits, both bands contained a strong preponderance of dislocations of the same sign, which would lead to rotations across the defect bands that are consistent with the observations made here.

While the defect patterns in the 'primary' and 'mixed' regions are plausible and consistent with Livingston's 'polygonized glide', it is difficult to explain the retention of this structure in the region of conjugate shear. Shear by the conjugate bands is certainly plausible. Even if these are made up of the same dislocations as the primary bands, as Livingston proposed, a perpendicular array of them would create a tilt boundary that is, in effect, a plane of conjugate shear. But this observation does not explain why a macroscopic band of conjugate should have a structure that is dominated by extended bands of, apparently, primary shear.

Given that the understanding of the conjugate shear will have to wait more detailed studies, such as the TEM studies that are now underway, three possibilities suggest themselves. First, the dislocation density that is revealed by the selected area diffraction done here is an excess dislocation density that produces a local rotation. It remains possible that much of the macroscopic strain is due to a balanced dislocation distribution

that cannot be inferred from the microrotation pattern. (We note that the Livingston-Basinski results suggest that this explanation is not true.) Second, the dislocations responsible for the conjugate strain may be so diffuse in their distribution that they contribute primarily to the diffuse background dislocation density rather than to the apparent defect bands. Third, the detailed evolution of the defect distribution in the conjugate region may be such that it produces a rather different strain on the way to a superficially similar pattern. (We note that the mesoscopic defect pattern shows where defects are, while the strain is a consequence of where they have been.)

4.3 Mesoscopic stress pattern

While there is prior work on the mesoscopic defect patterns in deformed Cu, the present work is, to our knowledge, the first to map the mesoscopic distribution of stress. The results have several interesting features.

First, the magnitudes of the residual shear stresses are surprisingly large (Figs. 13-16). Whether the shear stress is measured by the in-plane shear (σ_{yz}), the maximum resolved shear stress or the Von Mises stress, the shear stress reaches values of 500-1000 MPa, which is much higher than the nominal shear strength of the crystal. These high stresses are concentrated in the primary shear bands and, to a lesser extent, the conjugate shear bands (figs. 15,16,18). The fact that the maximum stresses appear to be in the defect bands, rather than adjacent to them, suggests that these high stresses are due to defect tangles and pile-ups that prevent their relaxation.

Second, the maximum shear stresses in the highly stressed, primary defect bands are in crystallographic directions that do not lie in the (111) plane of primary slip (Fig. 17). It follows that these stresses cannot be relaxed by primary slip, a fact that may play a strong role in their preservation in the relaxed crystal. On the other hand, the stresses in the regions between the primary shear bands are in the (111) glide plane (though not in the $[\bar{1}01]$ direction). Stresses in this plane should contribute to the polygonization of the dislocation in the spaces between the primary shear bands.

Third, a superposition of the maximum resolved shear stress and the dislocation density (Fig. 18) shows both the strong correlation between high shear stress and the primary defect bands, and the much weaker correspondence between high shear stress and the conjugate bands. The relatively frequent observation of conjugate defect bands in regions of low residual stress suggests that the conjugate defect bands tend to form, or deform so as to relax the local stresses.

5 Conclusion

The work reported here shows how ‘multiscale characterization’ can be used to clarify the nature and interaction of the heterogeneous deformation patterns and mechanisms that operate at different length scales. In the particular case studied here, the uniaxial compression of a copper single crystal oriented for single slip in the $(111)[\bar{1}01]$ slip system and tested to ~10% strain in uniaxial compression, optical ‘image correlation’ methods successfully mapped the strain field with a spatial resolution of about 100 µm. The macroscopic strain produced in an inhomogeneous pattern of broad, crossed shear bands in the x-face of the crystal, which was oriented perpendicular to $[1\bar{2}1]$ and contained the $[\bar{1}01]$ direction of the preferred slip system. One, the primary band, lay parallel to (111). The second, the ‘conjugate’ band, was oriented perpendicular to (111)

and contains no common slip plane of the fcc crystal. The two bands divided the crystal into distinct primary, conjugate and mixed (crossed primary and conjugate) regions. However, the mesoscopic substructure of the three regions was surprisingly similar. As determined by selected area synchrotron diffraction with a resolution of 1-3 µm, the dominant feature in all three regions was a quasi-periodic pattern of broad, somewhat irregular primary bands that lay nominally parallel to (111) with a period of about 30 µm. There were also broad conjugate defect bands, almost precisely perpendicular to the primary bands that tended to bridge primary bands and terminate at them. These were more common and pronounced in the region of conjugate strain. The measured residual shear stresses were large (ranging to well above 500 MPa) and strongly correlated with the primary shear bands. The direction of maximum stress in the primary bands was oriented out of the (111) glide plane. The maximum shear stresses between the primary defect bands were oriented in the (111) planes. While some of the conjugate defect bands had high shear stresses, others were almost devoid of shear stress, suggesting that the conjugate bands acted to relax the internal stress. The results are compared to the mesoscopic defect patterns found in Cu in etch pit studies done some decades ago. The results are being extended by high resolution TEM analyses, with particular emphasis on such puzzling questions as the nature of the conjugate bands and the mechanism that makes the macroscopic conjugate strain consistent with a mesoscopic pattern that is dominated by defect bands parallel to the plane of the primary macroscopic shear.

Acknowledgements

This work was performed under the auspices of the U.S. Department of Energy by University of California, Lawrence Livermore National Laboratory under Contract W-7405-Eng-48. The Advanced light Source is supported by the Director, Office of Science, Office of Basic Energy Sciences, of the U.S. Department of Energy under Contract No. DE-AC02-05CH11231 at Lawrence Berkeley National Laboratory

References

[1] B. Devincre and L.P. Kubin, Materials Science and Engineering A -Structural Materials Properties Microstructure and Processing **234** 8-14 (1997).
[2] W. Cai, V.V. Bulatov, T.G. Pierce, et al., *Massively-Parallel Dislocation Dynamics Simulations*, in *Solid Mechanics and Its Applications*, H. Kitagawa and Y. Shibutani, Editors. 2004, Kluwer Academic Publisher.
[3] D.H. Lassila, M.M. LeBlanc, and G.J. Kay, Journal of Engineering Materials and Technology-Transactions of the Asme **124** 290-296 (2002).
[4] D.H. Lassila, M.M. LeBlanc, and J.N. Florando, Metallurgical Transactions **accepted** (2006).
[5] C.R. Cupp and B. Chalmers, Acta Metallurgica **2** 803-809 (1954).
[6] E.N.D. Andrade, Proceedings of the Royal Society of London Series a-Mathematical and Physical Sciences **240** 304-& (1957).
[7] J.W. Steeds, Proceedings of the Royal Society of London Series a-Mathematical and Physical Sciences **292** 343 (1966).
[8] T. Ungar, H. Mughrabi, and M. Wilkens, Acta Metallurgica **30** 1861-1867 (1982).
[9] Z.S. Basinski and S.J. Basinski, Philosophical Magazine **21** 213-251 (2004).
[10] H. Mecking and G. Bulian, Acta Metallurgica **24** 249-260 (1976).
[11] J.D. Livingston, Journal of Applied Physics **31** 1071-1076 (1960).
[12] J.D. Livingston, Acta Metallurgica **10** 229-239 (1962).

[13] Z.S. Basinski and S.J. Basinski, Philosophical Magazine **9** 51 (1964).
[14] R.W. Cahn, Journal of the Institute of Metals **79** 129-158 (1951).
[15] E.A. Calnan, Acta Crystallographica **5** 557-563 (1952).
[16] R.W.K. Honeycombe, Journal of the Institute of Metals **80** 49 (1951).
[17] R.W.K. Honeycombe, Journal of the Institute of Metals **80** 45-49 (1951).
[18] D.H. Lassila, M.M. LeBlanc, and M. Rhee, Materials Research Society Symposium Proceedings **779** (2003).
[19] M.M. LeBlanc and D.H. Lassila, Experimental Techniques **20** 21-24 (1996).
[20] J.W. Dally and W.F. Riley, *Experimental Stress Analysis*. 4th ed. 2005, Knoxville: College House Enterprises, LLC.
[21] M.M. LeBlanc, J.N. Florando, D.H. Lassila, et al., Experimental Techniques **30** 33-37 (2006).
[22] D.P. Field, *Personal communication.* 2007.
[23] N. Tamura, A.A. MacDowell, R. Spolenak, et al., Journal of Synchrotron Radiation **10** 137-143 (2003).
[24] N. Tamura, R.S. Celestre, A.A. MacDowell, et al., Review of Scientific Instruments **73** 1369-1372 (2002).
[25] N. Tamura, A.A. MacDowell, R.S. Celestre, et al., Applied Physics Letters **80** 3724-3726 (2002).
[26] J.S. Chung and G.E. Ice, Journal of Applied Physics **86** 5249-5255 (1999).
[27] N. Tamura, H.A. Padmore, and J.R. Patel, Materials Science and Engineering a-Structural Materials Properties Microstructure and Processing **399** 92-98 (2005).
[28] J.F. Nye, Acta Metallurgica **1** 153-162 (1953).
[29] J. Florando, M.M. LeBlanc, and D.H. Lassila, Scripta Materialia **accepted** (2007).

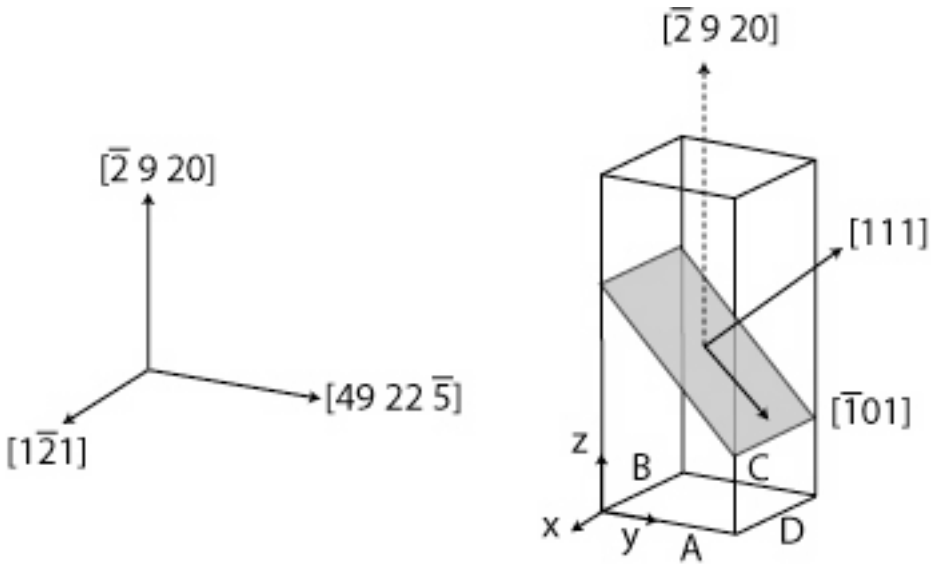

Fig. 1: The shape and orientation of the Cu test specimen.

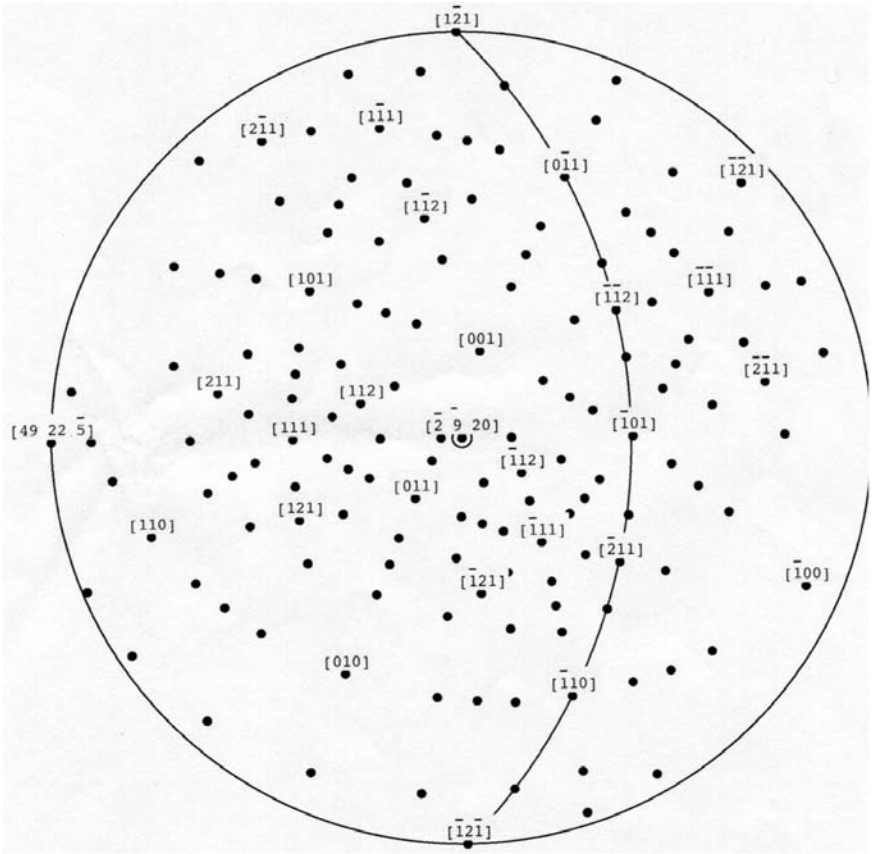

Slip System	Schmid Factor
(111), [-101]	0.50
(-111), [101]	0.47
(1-11), [011]	0.32
(-111), [0-11]	0.29
(111), [1-10]	0.25
(111), [0-11]	0.25
(1-11), [-101]	0.24
(-111), [110]	0.18
(-1-11)[011]	0.13
(-1-11)[101]	0.079
(1-11), [110]	0.077
(-1-11)[-110]	0.048

Fig. 2: Stereographic projection and tabulated Schmid factors for the crystal orientation shown in Fig. 1.

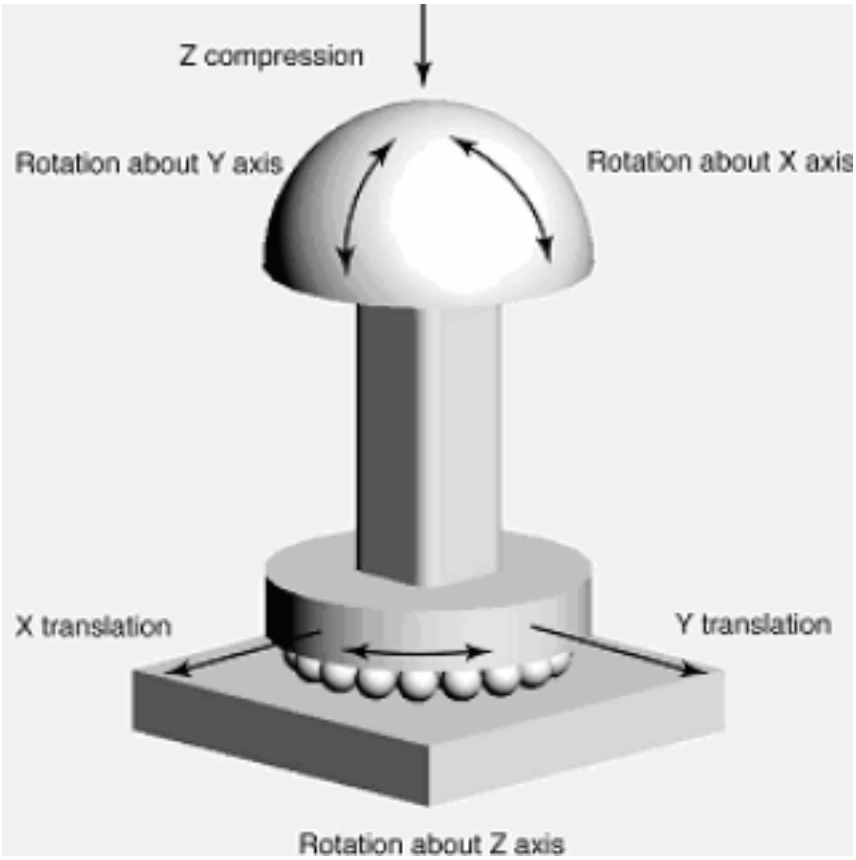

Fig. 3: Schematic of a compression test in the "6DOF" apparatus [1,2]. The objective is to allow unconstrained shape change. The six allowed deformation modes are translation in z (compression), translation in x or y (translation of the basal platen), rotation about x or y (tilt of the hemispherical upper platen) and rotation about z (rotation of the basal platen).

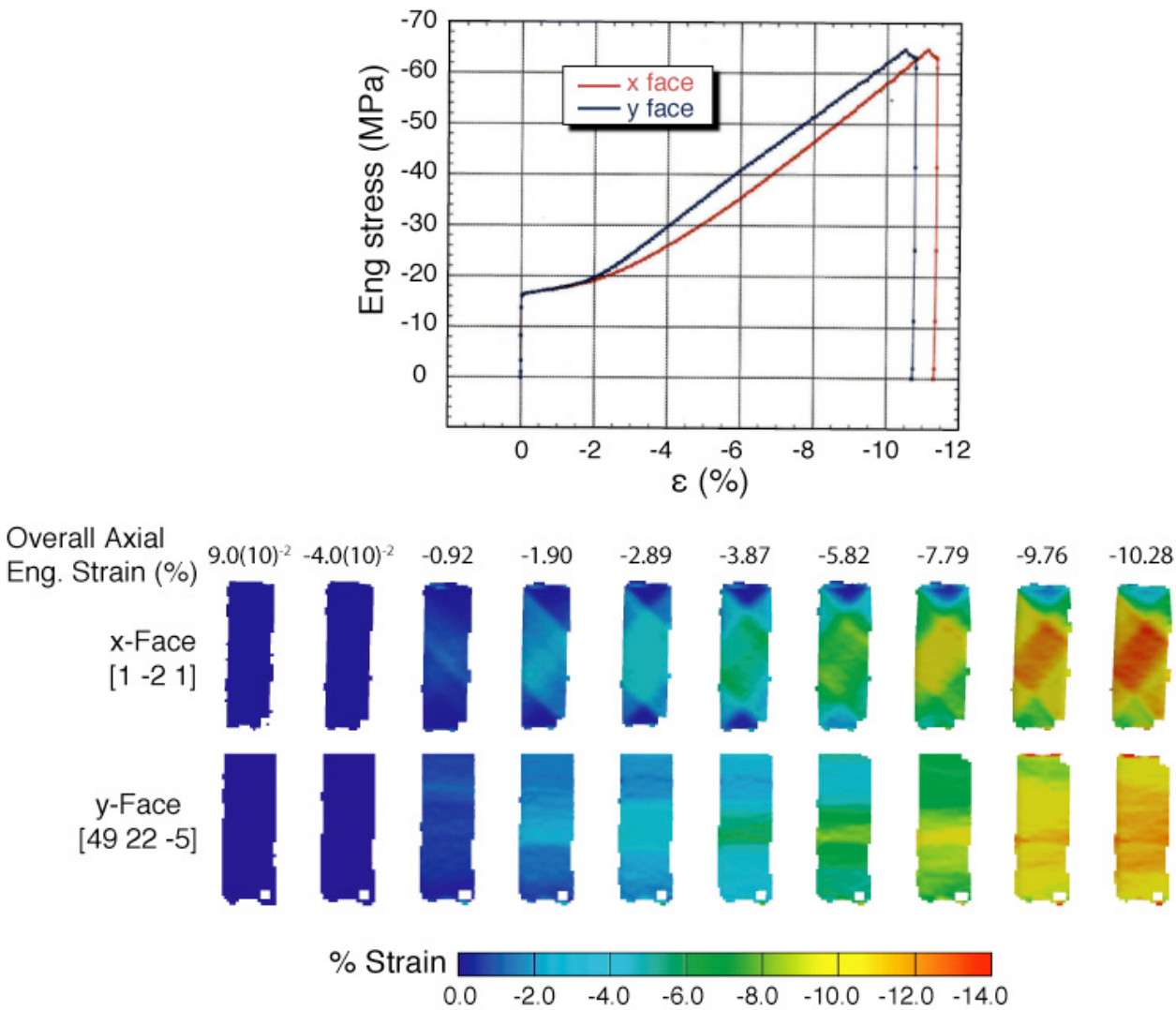

Fig. 4: A succession of images showing includes color-coded maps of the distribution of compressive strain (ε_{zz}) on the x- and y-faces as a function of the overall axial strain on the specimen.

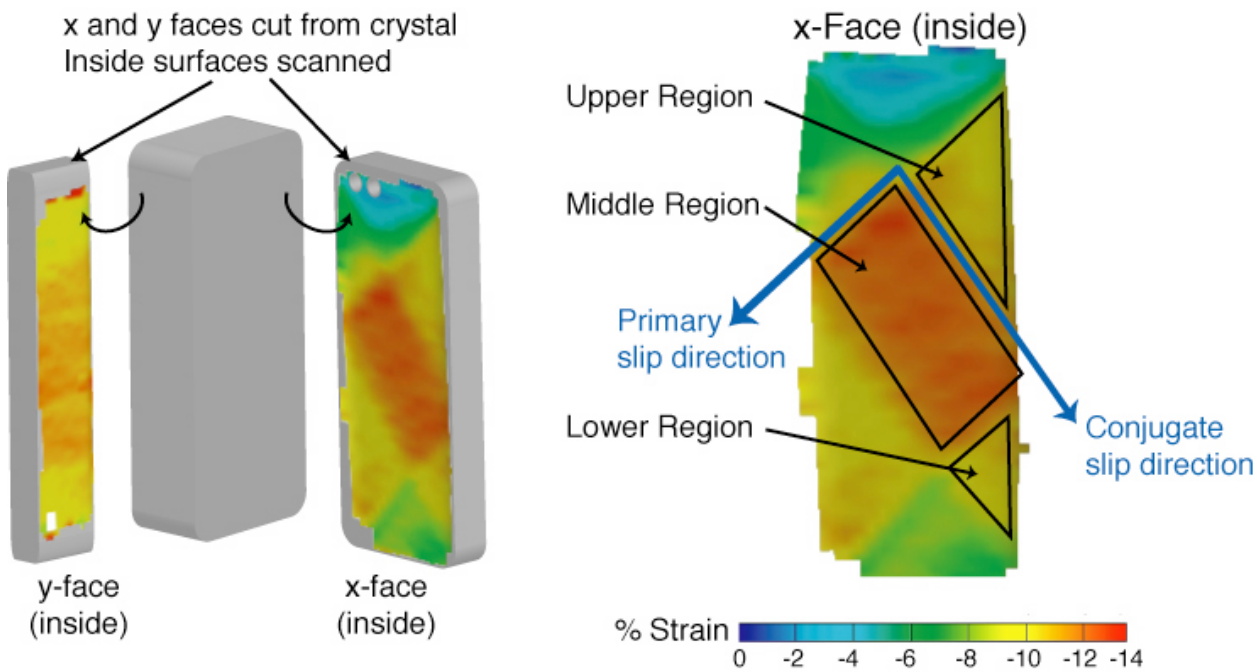

Fig. 5: The surfaces scanned were the inside surfaces of 1 mm thick slabs cut from the x- and y-faces. The distinct regions on the x-face are shown. Note the strain is a mirror image of that shown in Fig. 4.

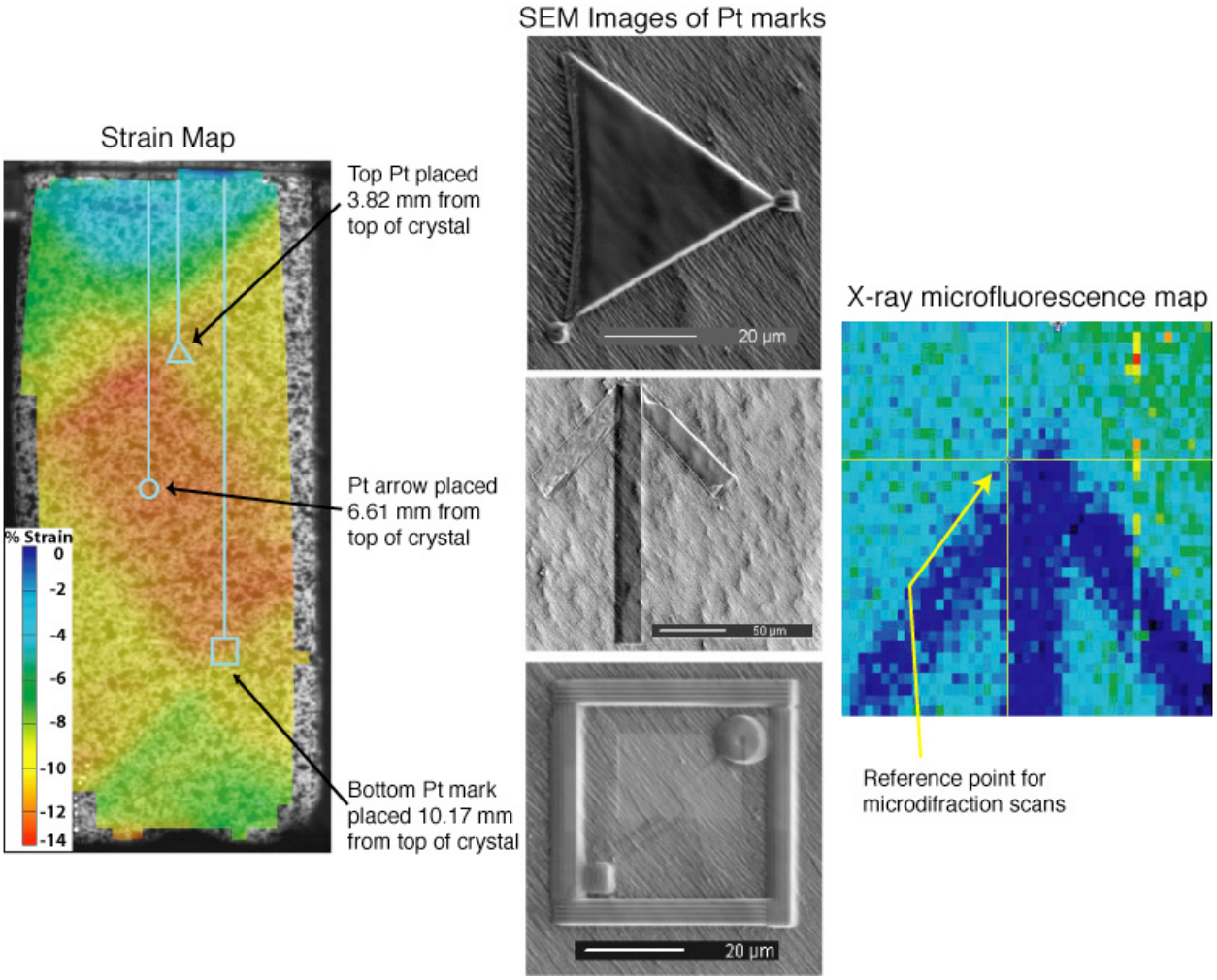

Fig. 6: The image correlation strain map with locations of platinum markers shown. SEM images of the three platinum markers are shown, along with the x-ray microfluorescence map of the platinum arrow (central marker) taken on the beamline.

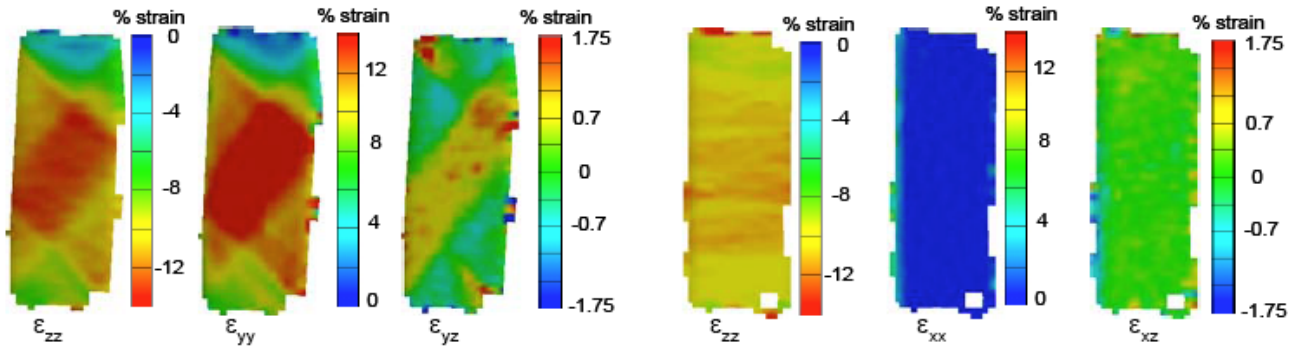

x-face y-face

Fig. 7: Maps of the strain fields in the x- and y-faces.

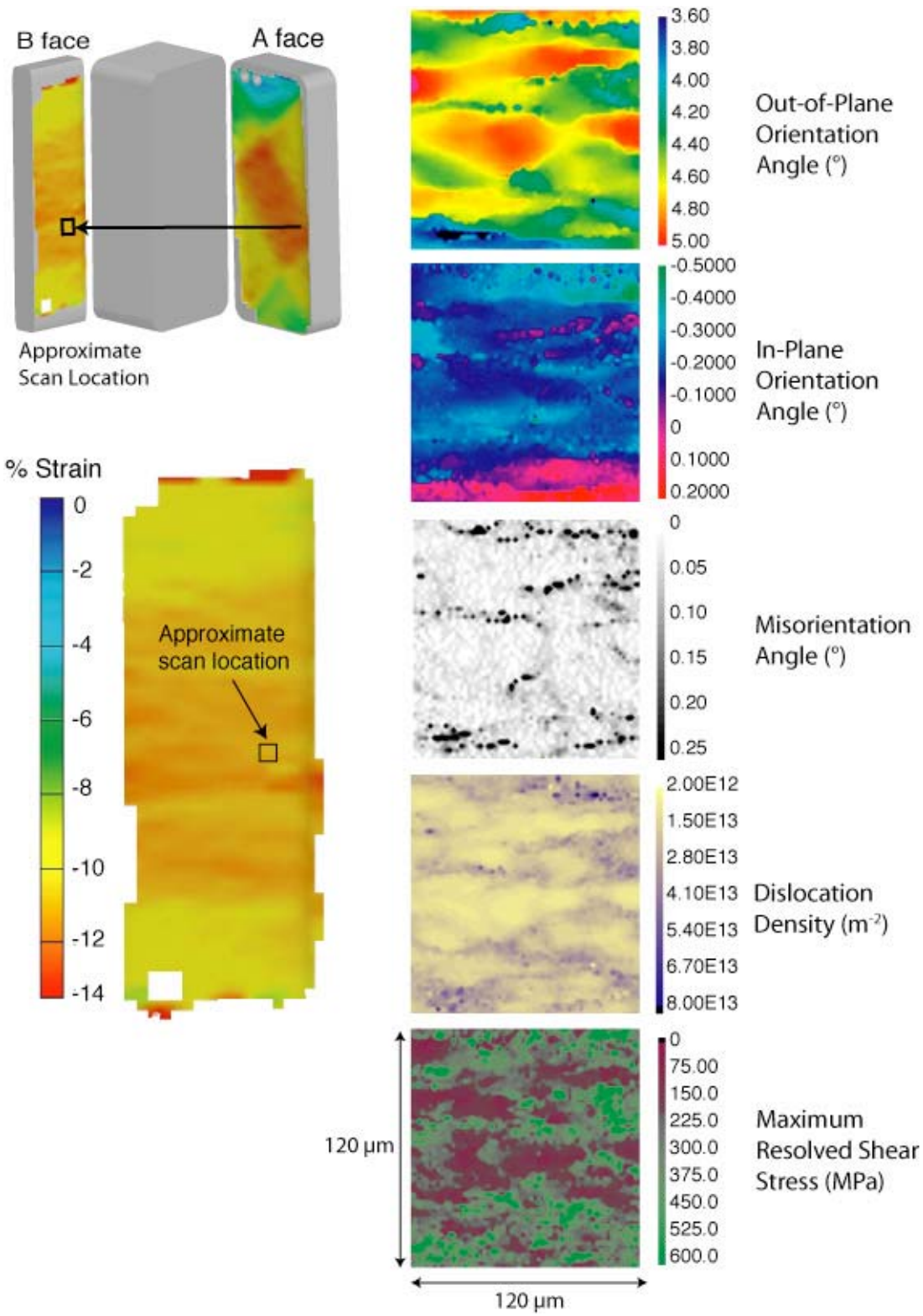

Fig. 8: Microdiffraction maps from the y-face, taken with 2-micron step size. The approximate location on strain maps is noted. Note that the bands of high dislocation density superimpose on gradients in the out-of-plane orientation.

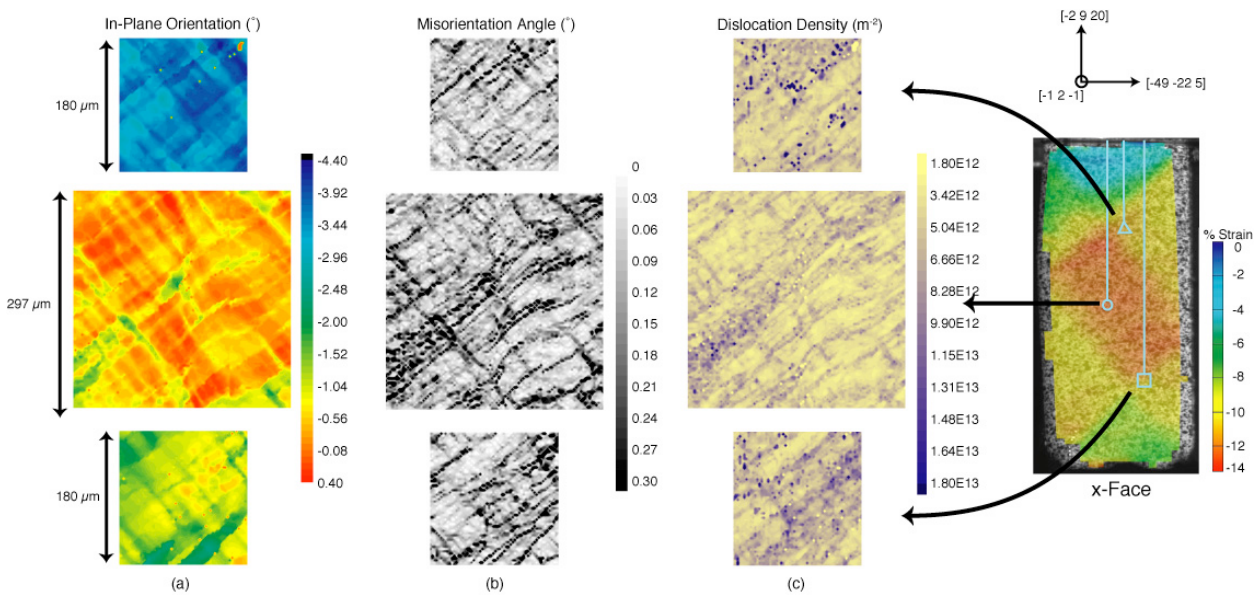

Fig. 9: Maps from large area scans in 3 regions noted in strain map: (a) dislocation density maps, (b) in-plane misorientation angle maps and (c) in-plane orientation. Orthogonal sets of parallel bands of high dislocation density and large misorientation are seen throughout the crystal.

.

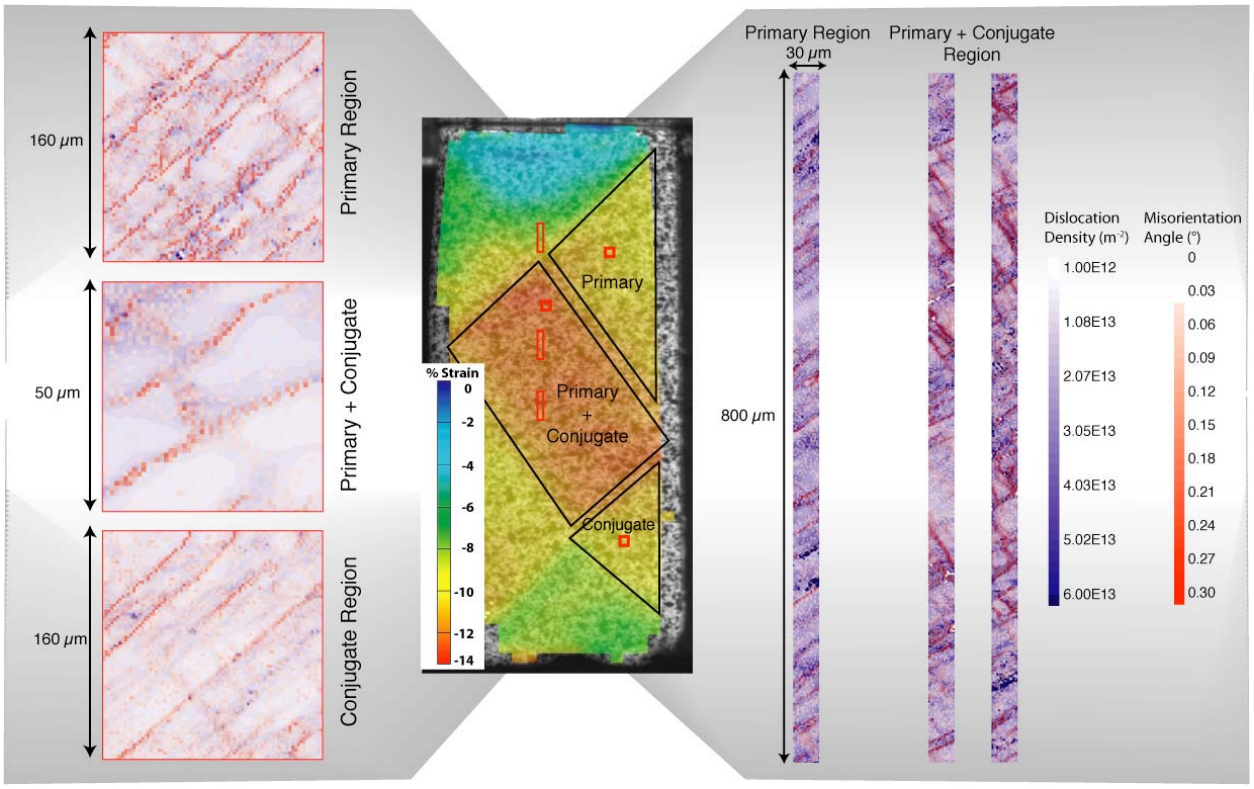

Fig. 10: Maps of misorientation angle superimposed on maps of dislocation density to demonstrate suitability of dislocation density approximation. This approximation calculates the dislocation density from the average peak-width assuming the peak spreading is caused by lattice curvature due to excess same-sign dislocations. The square area scans are taken from each of the strained regions of the crystal, and the strips of surface mapped are 800x30 μm^2, one taken from the primary deformation band, two from the region of mixed primary and conjugate deformation.

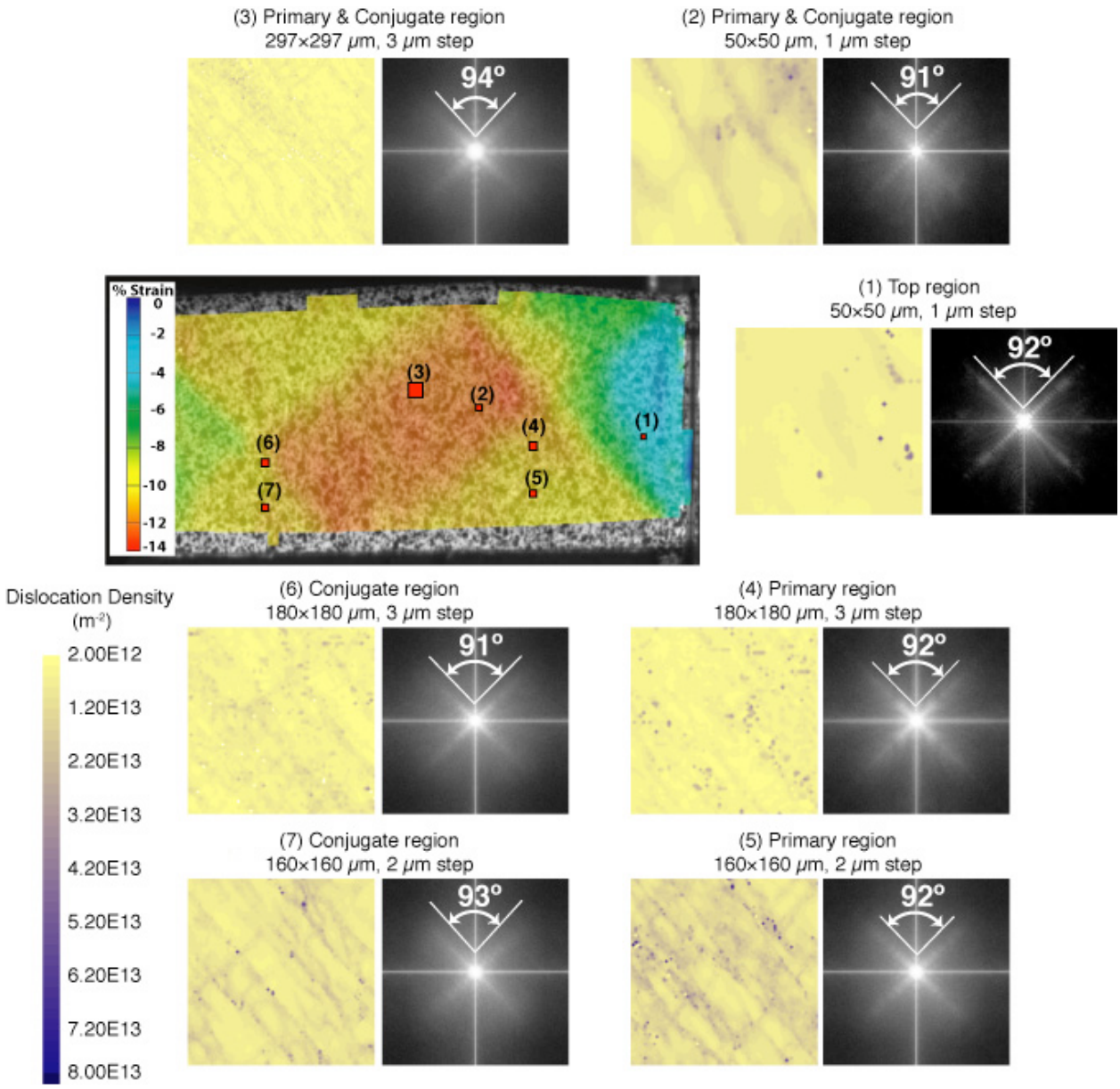

Fig. 11: Maps of dislocation density from x-ray microdiffraction results and corresponding Fourier transforms of each map. The angle of intersection between the primary and conjugate is approximately 90 degrees in all regions of the crystal.

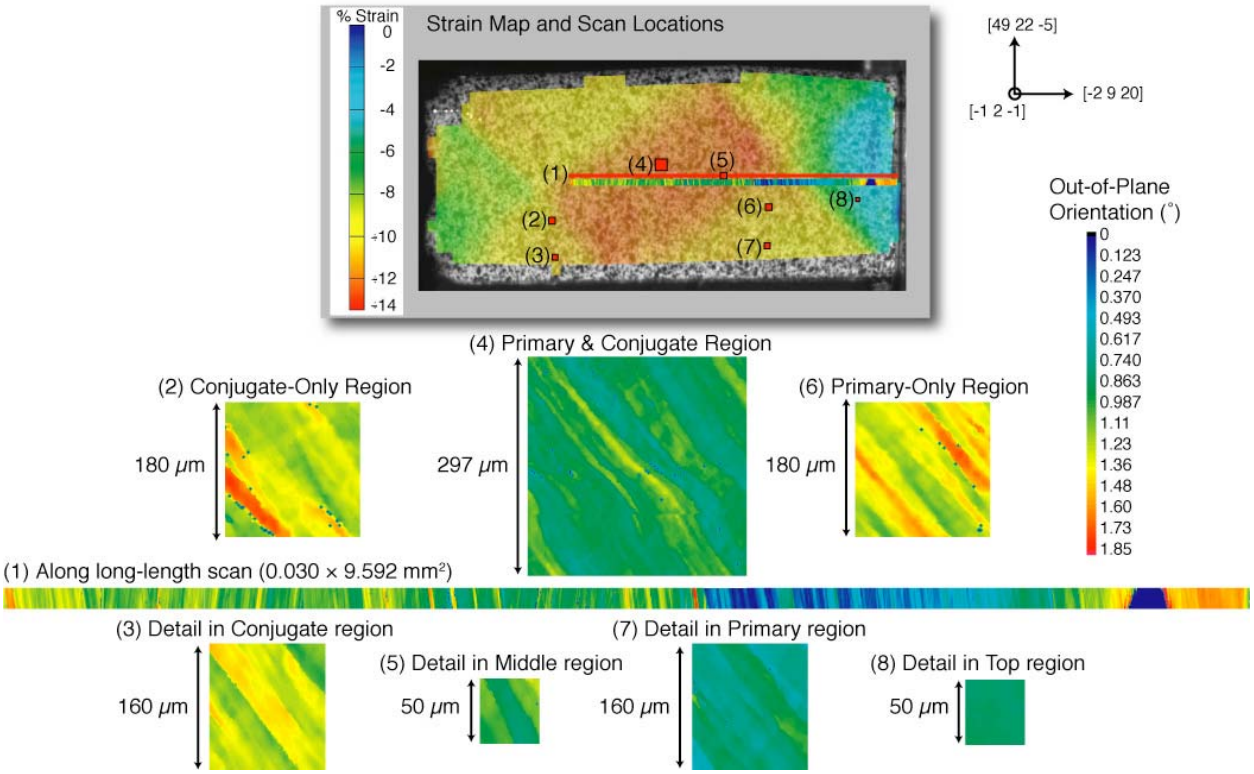

Fig. 12: Out-of-plane orientation maps from area scans and long-length scan linked to locations on strain map. Scans (2), (4) and (6) were taken with a 3 μm step-size; scans (1), (3), (7), and the long-length scan with a 2 μm step-size; and scans (5) and (8) with a 1 μm step size. The long scan down the length of the crystal shows

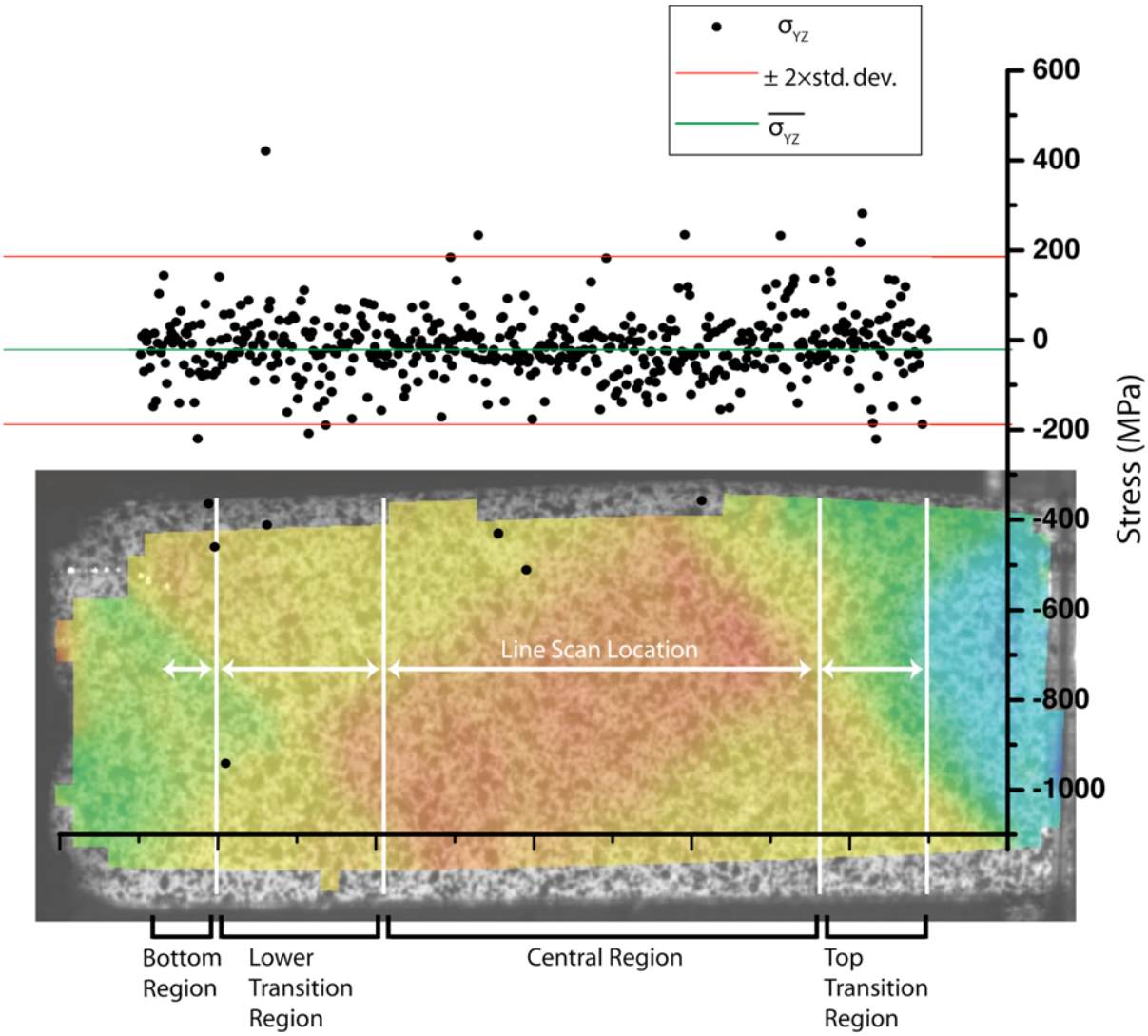

Fig. 13a: (a) Plot of the in-plane shear stress in the x-face (σ_{yz}) at 20 μm intervals along the line drawn in the crystal. The compressive strain map is in the background for reference. The stress scatters over several hundred MPa; the "2σ" limits are drawn. (b) The distribution of shear stress values from the line scan shown.

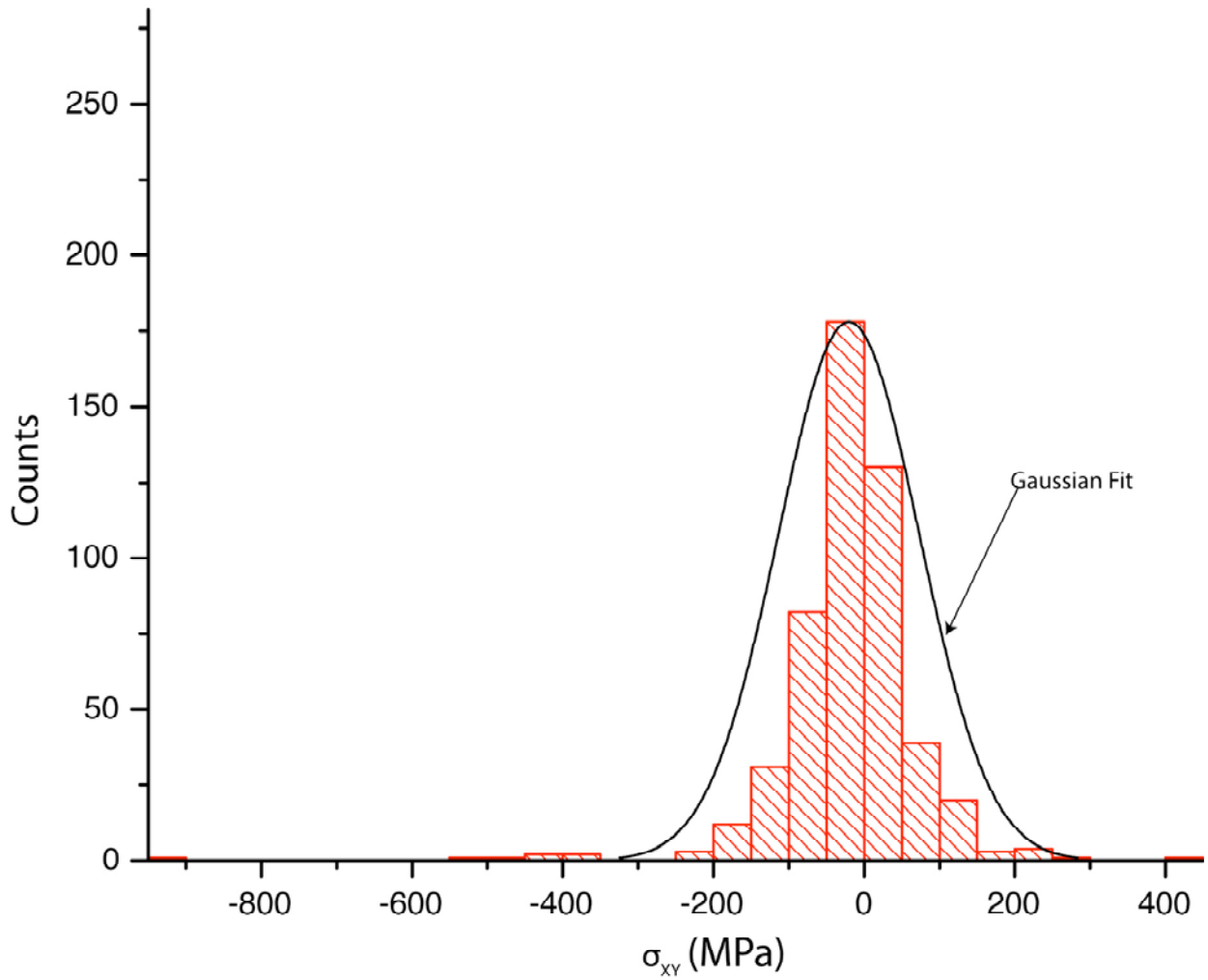

Fig. 13b: (a) Plot of the in-plane shear stress in the x-face (σ_{yz}) at 20 μm intervals along the line drawn in the crystal. The compressive strain map is in the background for reference. The stress scatters over several hundred MPa; the "2σ" limits are drawn. (b) The distribution of shear stress values from the line scan shown.

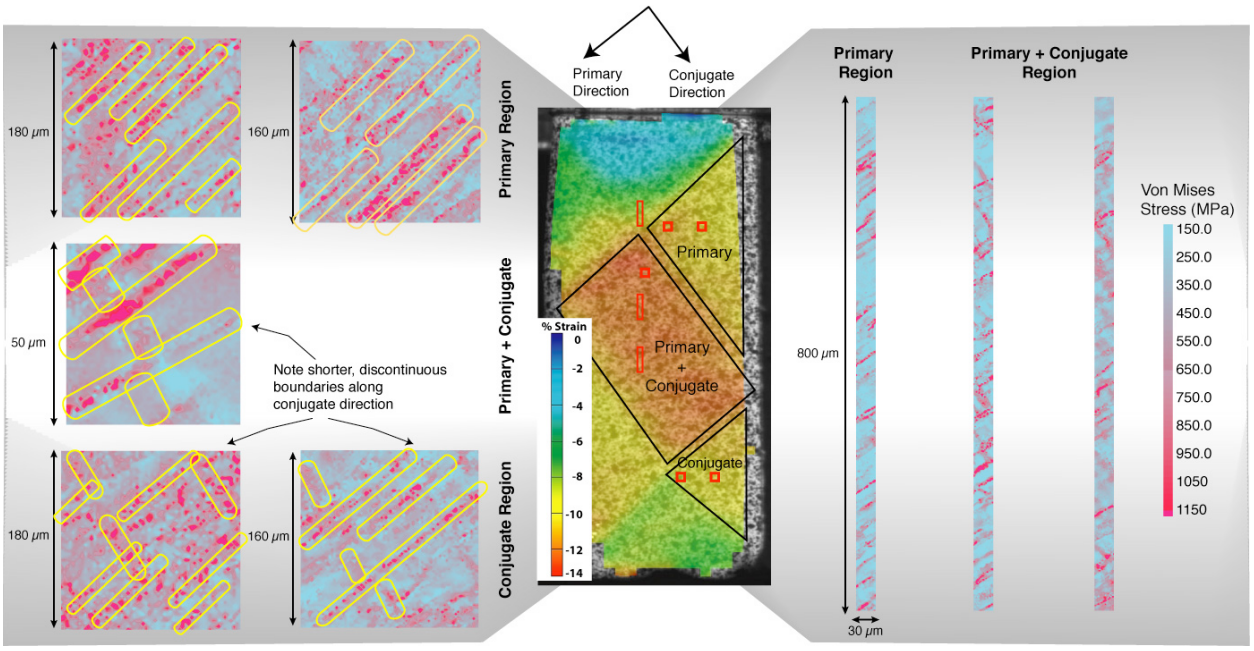

Fig. 14: Maps of the Von Mises shear stress over small areas of the x-face taken from the primary, primary + conjugate, and conjugate strain regions. and over 30x800 μm strips on the x-face taken from the primary, and primary + conjugate regions. Note that the measured residual shear stress reaches 1 GPa.

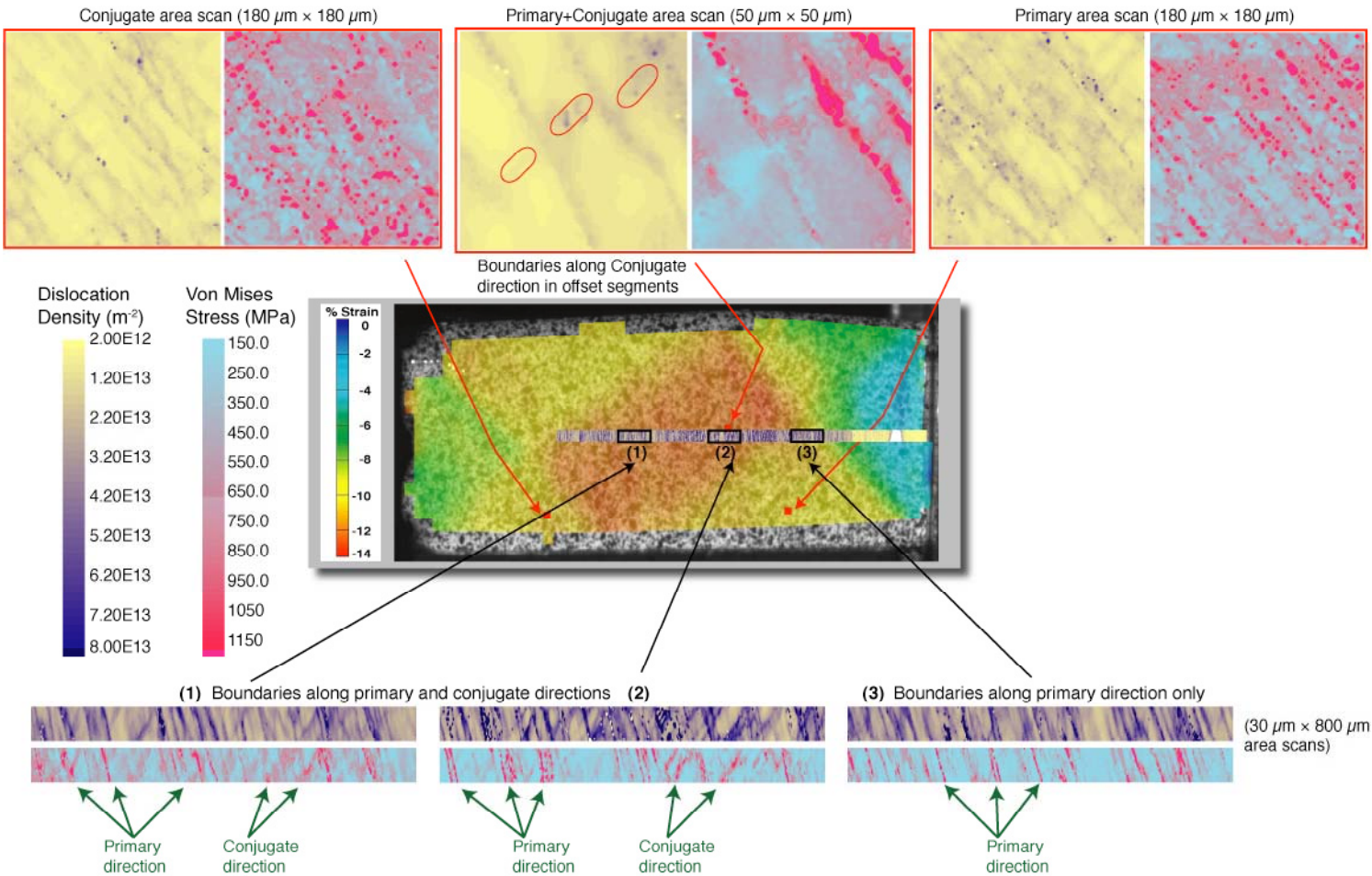

Fig. 15: Comparative maps of the average dislocation density and Von Mises stress for the three regions of strain in the crystal. Bands of high stress and high dislocation density superimpose clearly for the primary shear bands. The superposition is present, but less obvious for the conjugate shear bands.

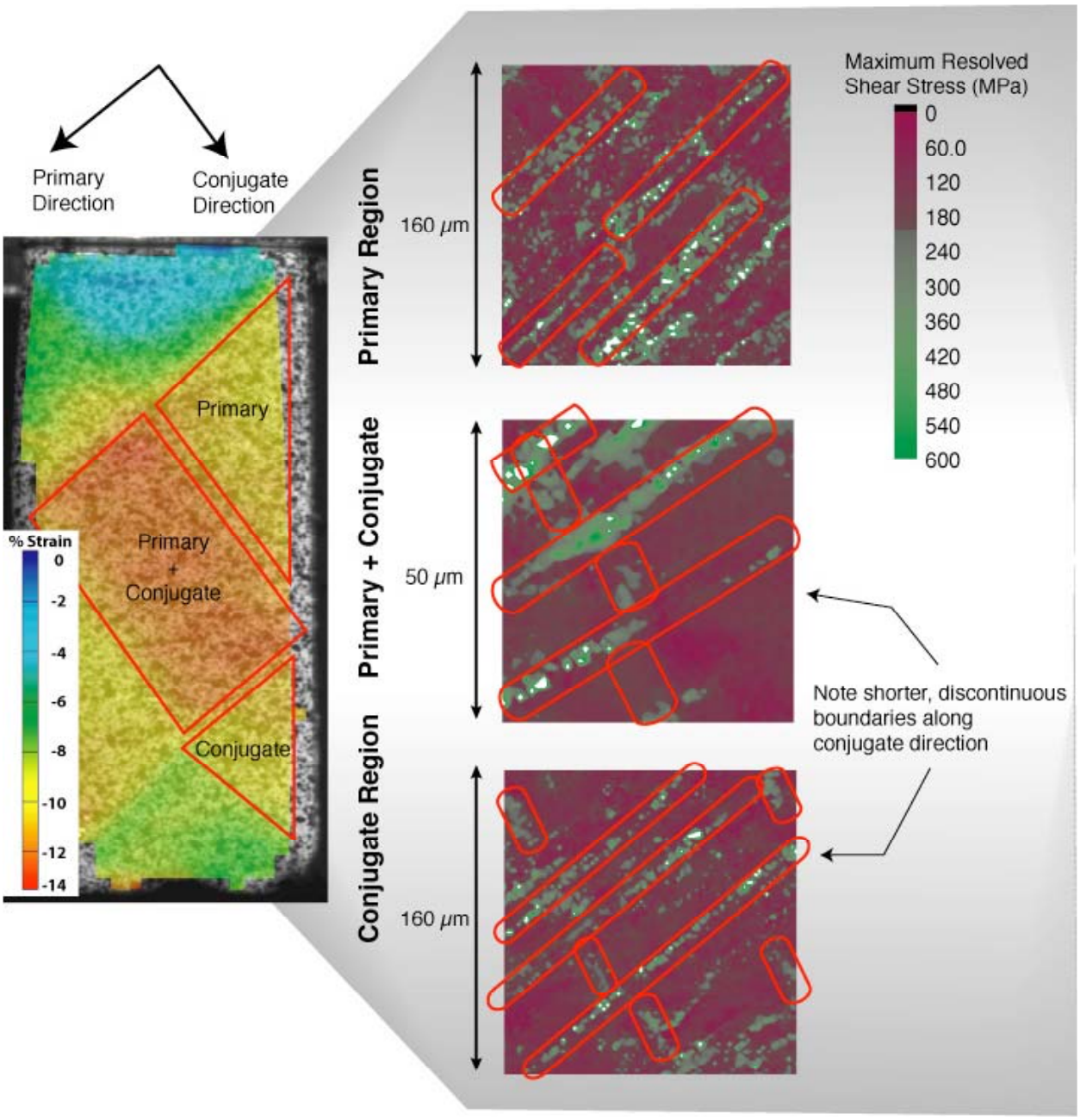

Fig. 16: Maps of the maximum resolved shear stress over regions taken from the primary, primary + conjugate and conjugate shear regions. Note that the bands of maximum stress that parallel bands of conjugate shear are relatively diffuse and discontinuous.

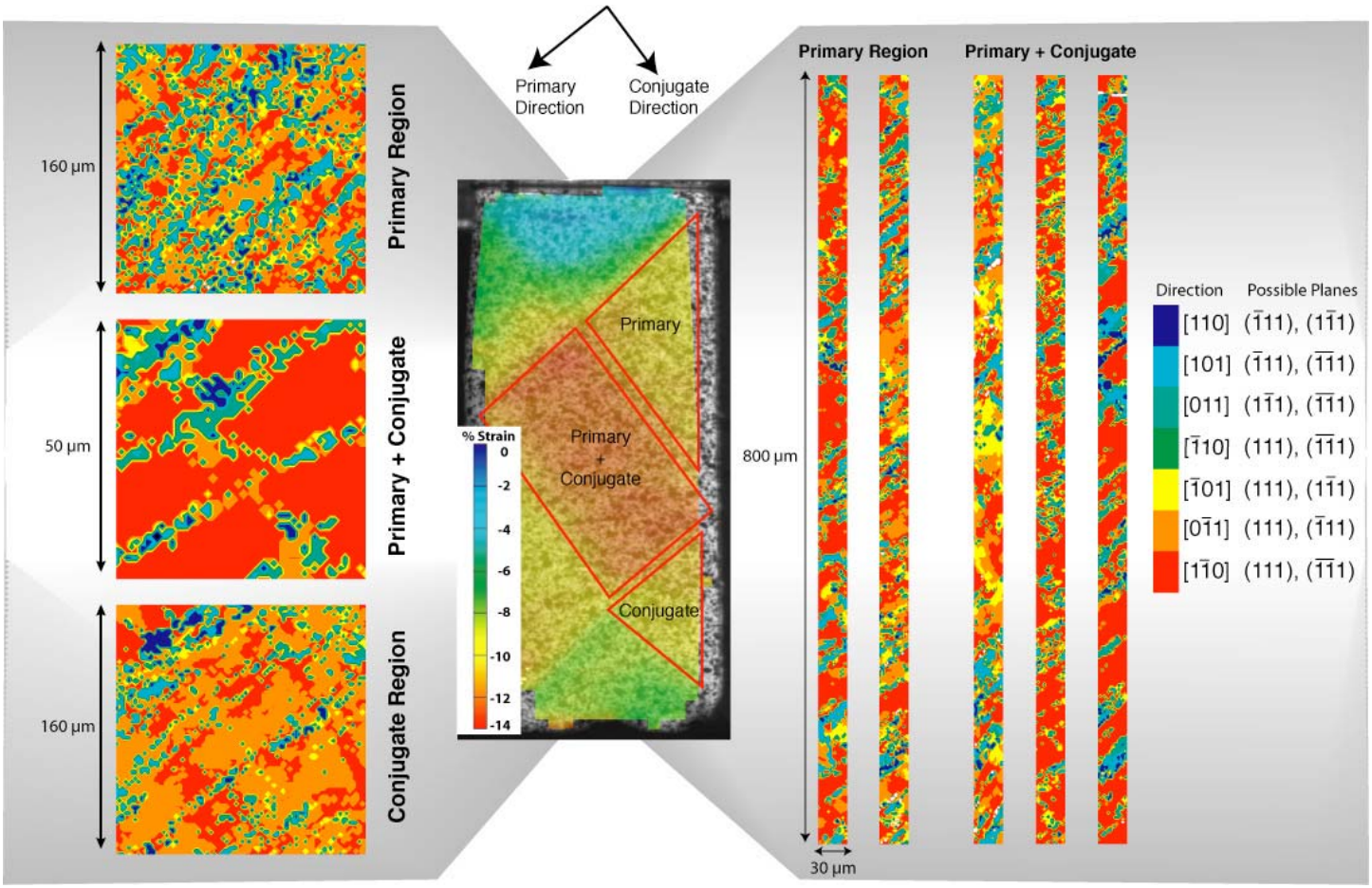

Fig. 17: Maps of the crystallographic direction of the maximum resolved shear, along with the possible planes that may contain this direction. Note that the highest stresses lie in bands parallel to the primary (111) slip planes, but in directions that are not contained in these planes.

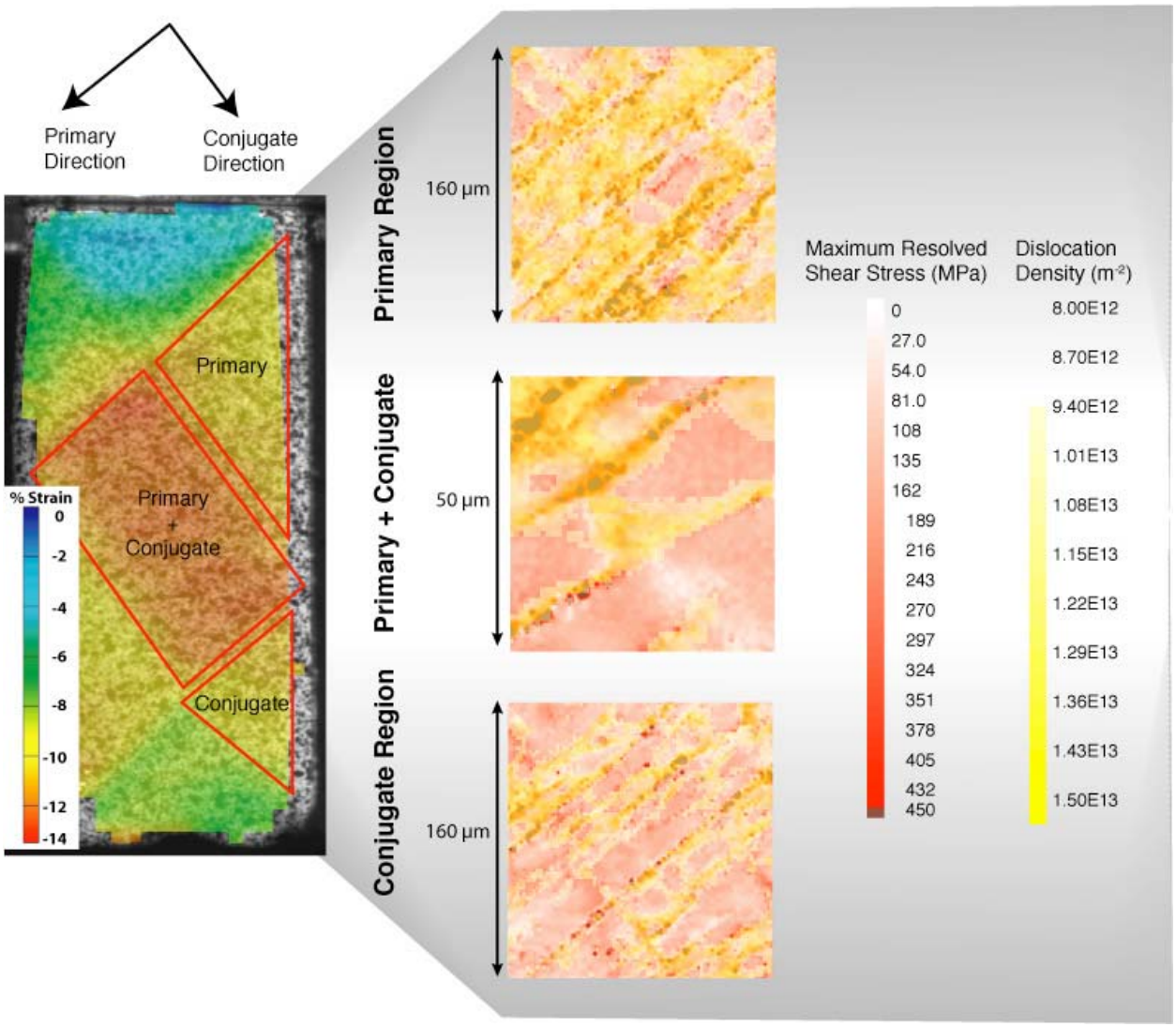

Fig. 18: Dislocation density maps overlaid on MRSS maps, demonstrating correspondence between high dislocation density and maximum shear stresses indicating that the dislocations are imposing the shear stresses rather than relaxing them.